Semester-Thesis

The Influence of Wire-bonds on Coplanar Waveguide Resonators

Presented by: Adrian Stalder
Supervisor: Lars Steffen
Prof. Dr. Andreas Wallraff
Quantum Device Lab
Laboratory for Solid State Physics
ETH Zurich

Zurich, February 2, 2010

ETH
Eidgenössische Technische Hochschule Zürich
Swiss Federal Institute of Technology Zurich

Abstract

One of the main components of a circuit QED system is the coplanar waveguide resonator. In new chip designs, additional control lines divide the ground planes in several non-connected parts. These discontinuities give rise to parasitic resonances in the resonator spectrum. In this report the influence of wire-bonds placed in different locations on the chip to connect the different ground planes is studied. The influence on the quality factor as well as resonances throughout the whole spectrum is analysed.

In general a smoothening of the spectrum is observed as well as an increase in the quality factor due to the bonding. The data collected can be used for the further analysis in specific cases to study the possible influence of additional bonds.

Contents

Chapter 1

Introduction

1.1 Motivation

Computation in omnipresent in todays world through personal computers, mobile devices or other technical gadgets. The computers get faster and smaller every blink of an eye. Gordon Moore, an Intel co-founder, predicted in 1965 a doubling of the transistor density on a processor every two years. This prediction holds until today but how long can it proceed at this speed? It can be shown with simple calculations that the physical limit will be reached in 2036 [1] but the quantum regime will be approached in the early 2020's. As a concequence researchers are looking for alternatives to classical computation as we know it and one of these apporaches is quantum computation.

1.2 Classical Computation

Compuation with bits is based on classical physical laws. Classical information is sotred in bits which can take the value 0 or 1. A possible representation of a bit is a low (logical 0) and high (logical 1) voltage in the Transistor-Transistor-Logic. Logical gate operations can be realized using transistors or diodes and can be combined to integrated circuits performing complicated algorithms. Any classical logical gate can be decomposed into a circuit of NAND gates, making it a universal gate of classical computation.

The universal gates are especially important for new computational setups because if the universal gate can be implemented, any operation can be implemented.

A	B	A NAND B
0	0	1
0	1	1
1	0	1
1	1	0

Table 1.1: Truth table of the NOT AND gate (NAND).

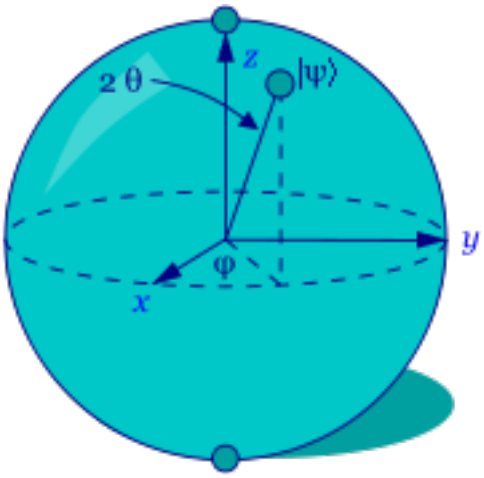

Figure 1.1: Bloch sphere representation of a qubit. [2]

1.3 Quantum Computation

New principles of computation need to have advantages over classical computation. Usually better means faster, less power consumption or smaller. What are the analogs to a classical bit, logical gates and integrated circuits for quantum computation and what are their advantages over their classical counterparts?

1.3.1 Qubit

The quantum mechanical analog to the classical bit is the quantum bit, short qubit. The qubit is a very similar concept to the classical bit. It consists of the two computational basis states |0> and |1>, which are orthogonal to each other. Unless the classical bit the qubit it can be in both states at the same time, in a so-called superposition state. The mathematical describtion of a qubit state is the given by

$$|\psi >= \alpha|0 > +\beta|1 >= \cos(\theta)|0 > +e^{i\phi}\sin(\theta)|1 > \tag{1.1}$$

where α and β are complex numbers with $|\alpha|^2 + |\beta|^2 = 1$. The measurement of a qubit gives with probability $|\alpha|^2$ ($|\beta|^2$) the result |0> (|1>). To visualize a single quibit it is useful to introduce the Bloch sphere (see Fig. 1.1). The angles θ and ϕ from the second part of Eq. 1.1 define the point on the three dimensional sphere. There would be an additional global phase which can be omitted.

1.3.2 Quantum Gates

Analog to the classical logical operations there exist quantum gates. Quantum gates can be represented as matrices acting on the states represented as vectors. For example

$$|0 >= \begin{pmatrix}1\\0\end{pmatrix}, |1 >= \begin{pmatrix}0\\1\end{pmatrix} \tag{1.2}$$

Input state	Output state
|00>	|00>
|01>	|01>
|10>	|11>
|11>	|10>

Table 1.2: Truth table of the quantum mechanical Controlled NOT gate (CNOT).

is a possible representation. Single qubit gates can be understood as rotations around certain axes in the bloch sphere representation and can easily be written in terms of matrices. For universal quantum computation in addition to the single qubit gates there are also two-qubit gates needed. All quantum gates need to be reversible which is a major difference to classical gates. One example for a universal two-qubit quantum gate is the Controlled NOT gate, see Tab. 1.2.

With these instruments available quantum circuits can be realized to perform quantum algorithms.

1.3.3 Quantum Algorithms

With the discovery of quantum algorithms which are faster than their classical analogs, the interest in the field started to grow not only inside the physics community. The doubtless most stimulating algorithm was Shor's algorithm which solves the factoring problem with a exponential speedup over the best known classical algorithms[1]. Shor's algorithm became a lot of attention and mobilized a lot of money due to the fact that todays cryptography is based on the complexity of the factoring problem. RSA for example is a very well known public-key cryptography algorithm which bases on the multiplication of two prime numbers. To crack this code with a classical computer is extremely time consuming but would be a matter of seconds with a quantum computer. This drew the attention of governments and especially their secret services to quantum computation. Another important quantum algorithm is Grover's algorithm implementing quantum search providing a quadratic speedup over the best possible classical algorithm.

Richard Feynman was also involved in the discussion and pointed out the problem of classical computers simulating quantum mechanical systems. He saw in the simulation of quantum mechanical systems one of the main applications of a possible quantum computer. Considering that quantum mechanics has a far reaching influence on problems in other disciplines, e.g. explaining photosynthesis [3], this seems to be a major application. Arthur Ekert was recently asked by BBC what he thinks will be the major applications of quantum computers. In his view they will not be used in run-of-the-mill desktop applications but specialist uses such as searching vast databases, creating uncrackable ciphers or simulating the atomic structures of substances. "The really killer application will probably be in designing new materials or complex systems," he said [4].

[1] There is no proof that the fastest known classical algorithm indeed is the fastest possible classical algorithm.

1.3.4 Experimental Quantum Computer

There are different approaches for the experimental implementation of a quantum computer. David DiVincenzo summarized the criteria for an experimental implementation of a quantum computer into five points.

- Scalable physical system with well-characterized qubits
- Ability to initialize the state of the qubit
- Relatively long decoherence time compared to the gate operation time
- A universal set of quantum gates
- A qubit-specific measurement capability

Fulfilling all criteria is studied in many different experimental setups. The most promising seem to be superconducting circuits, quantum dots, ion traps, photons and nuclear magnetic resonance. Superconducting circuits fulfill the criteria pretty well and further improvement for example of the decoherence time should be seen in the near future.

1.4 Circuit Quantum Electrodynamics

From Quantum Electrodynamics (QED) we know that light can interact with matter. We are looking at an electromagnetic field which is induced by a photon in a cavity. This can interact with the electron states of an atom and excite (de-excite) them. This interaction is due to a transfer of an energy quanta. Cavity QED studies this interaction between light and atoms in resonant cavities. The particular field of looking at 1D transmission line resonators instead 3D cavities was introduced by Alexandre Blais et al. [5] and experimentally demonstrated by Andreas Wallraff et al. [6] in 2004 and is nowadays known as circuit QED.

In 1D the mode volume is smaller which leads to large electrical fields and leads to the strong coupling regime. That means that the timescale of the interaction is much faster than the decay into the environment. The circuit as well as the cavity QED system is described by the Jaynes-Cummings Hamiltonian

$$H = \hbar\omega_r(a^\dagger a + \frac{1}{2}) + \frac{\hbar\omega_a}{2}\sigma^z + \hbar g(a^\dagger\sigma^- + a\sigma^+) + H_\kappa + H_\gamma \tag{1.3}$$

where ω_r is the resonance frequency of the cavity, $a^\dagger$ and a the creation and annihilation operators of the electromagnetic field, ω_a the transition frequency of the atom, g the coupling strength between the field and the atom, σ^+ and σ^- the creation and annihilation operator of the atom. H_κ and H_γ represent the coupling of the cavity and the atom to the environment.

The coupling strength g depends on the detuning $\Delta = \omega_a - \omega_r$. For large detuning the two systems can be considered separately, but for a small Δ the field and the atom are entangled. In the setup at hand we do not have an atom but an artificial atom. There are several possibilities to realize an artificial atom for example the Cooper pair box as well as its enhancement the transmon qubit.

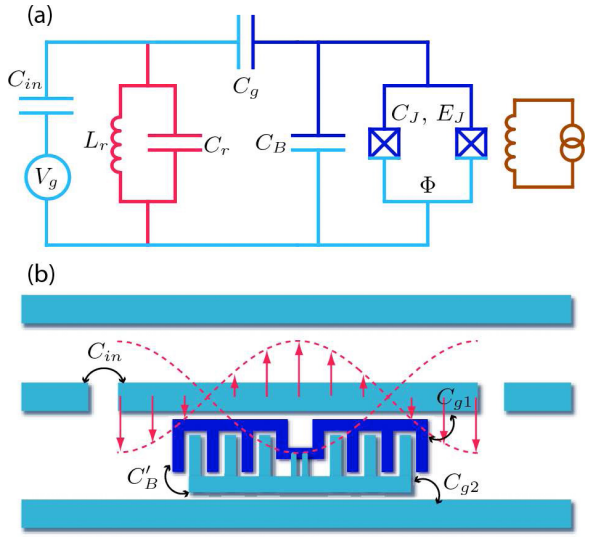

Figure 1.2: (a) Effective circuit diagram of the transmon qubit. The two Josephson junctions (with capacitance and Josephson energy C_J and E_J) are shunted by an additional large capacitance C_B, matched by a comparably large gate capacitance C_g. (b) Simplified schematic of the transmon device design (not to scale), which consists of a traditional split Cooper-pair box, shunted by a short (L $\sim \lambda/20$) section of twin-lead transmission line, formed by extending the superconducting islands of the qubit. This short section of line can be well approximated as a lumped-element capacitor, leading to the increase in the capacitances C_{g1}, C_{g2} and C'_B and hence in the effective capacitances C_B and C_g in the circuit. [9]

1.4.1 Transmon Qubit

The transmon is an improved superconducting charge qubit derived from the Cooper pair box [7, 8]. It is immune to charge noise without making it more susceptible to flux or critical current noise. The transmon consists of two superconducting island coupled through two Josephson tunnel junctions which are isolated from the rest of the circuit. In this setup Cooper pairs can tunnel between the two islands. The governing energies are the Josephson energy $E_J = E_{J,max}|cos(\pi\phi/\phi_0)|$ and the charging energy $E_C = e^2/2C_\sum$, with the external magnetic flux ϕ and the sum of all capacitances $C_\sum$. An illustration of the transmon can be seen in Fig. 1.2.

1.5 Coplanar Waveguide Resonators

The cavities used in the experiment are superconducting coplanar waveguide (CPW) resonators which can be routinely produced and have well defined properties.

The properties of a coplanar wave guide resonator are characterized by its series of resistance R* and inductance L* as well as its shunt capacitance C* and conductance G* per unit length. From mapping the trasmission line resonance

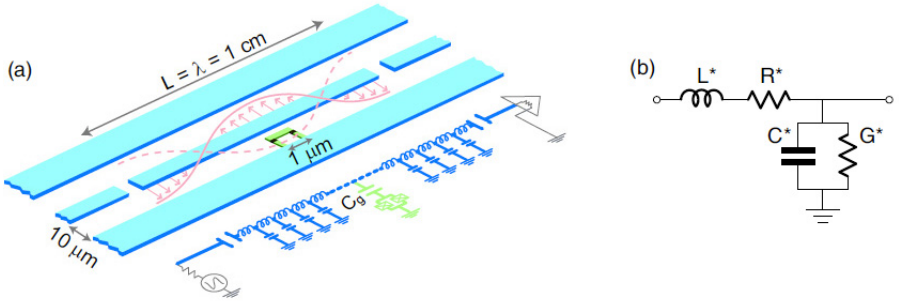

Figure 1.3: (a) Sketch of a coplanar waveguide resonator with a Cooper pair box as an artifical atom. (b) Transmission line resonator circuit model with input and output ports. [10].

to a LC resonator one gets [10]

$$\begin{aligned} R &= \frac{Z_0}{\alpha l}, \\ C &= \frac{\pi}{2\omega_0 Z_0}, \\ L &= \frac{1}{\omega_0^2 C} = \frac{2Z_0}{\pi\omega_0}, \end{aligned}$$

where Z_0 is the is the impedance of a lossless line, α the attenuation constant (real part of the propagation constant γ), β the imaginary part of the propagation constant γ and ω_0 fundamental resonance frequency. The quality factor can now be written as

$$Q = \omega_0 RC = \frac{\pi}{2\alpha l} = \frac{\beta}{2\alpha}. \tag{1.4}$$

In our case we have a capacitive coupling to an input and output which is shown in Fig. 1.3 (a). This gives rise to an external quality factor

$$Q_{ext} = \frac{n\omega_n C}{G_{ext}}, \tag{1.5}$$

with $G_{ext} = \frac{R_L C_\kappa^2 \omega_n^2}{1+R_L C_\kappa^2 \omega_n^2}$. R_L is the load resistor and C_κ the coupling capacitance for an input or output. Considering a symmetrical setup of input and output the external quality factor is given by $Q_{ext} = \frac{\omega_n nC}{2G_{ext}}$. The external quality factor is proportional to $\frac{1}{n}$ and more importantly proportional to $\frac{1}{\omega_0^2}$. The total loaded quality factor of the resonator is given by

$$\frac{1}{Q_L} = \frac{1}{Q_{int}} + \frac{1}{Q_{ext}}, \tag{1.6}$$

with $Q_{int} = \frac{n\omega_n C}{G_{int}}$. Incase one quality factors is much larger than the other, the smaller one can be neglected. From the internal and external quality factor we can define the coupling coefficient

$$g = \frac{Q_{int}}{Q_{ext}} = \frac{G_{ext}}{G_{int}}. \tag{1.7}$$

For the determination of the quality factor from a experimental dataset we use a Lorentzian line fitting

$$f(\nu) = A_0 \frac{\delta\nu_0/\pi}{(\nu - \nu_0)^2 + \delta\nu_0^2} \tag{1.8}$$

to the measured power spectrum. The quality factor is determined from the fundamental frequency ν_0 and the full width at half maximum $2\delta\nu_0$ as follows

$$Q = \frac{\nu_0}{2\delta\nu_0}. \tag{1.9}$$

1.6 Wire-bonds

Wire-bonding is the main process to interconnect integrated circuits with printed circuit boards. This is used in the setup of this experiment to connect the ground planes as well as the connectors with the PCB board. Additionally they are used in the setup to overcome the problem of a uniform grounding of the planes which arises due to additional lines. In different stages a set of wire-bonds over selected charge lines on the chip were attached. Wire-bonds are very convenient because they are easy to attach with a wire bonder which is available in the FIRST clean room at ETH.

1.7 Goal of the thesis

With more complex chip designs, which involve for example gate lines, a new problem evolved. An increasing amount of ground planes can influence the performance of the cavity due to voltage differences in the ground planes. The approach in this work is to add aluminium wire-bonds at several places on the chip and observe its influence on the spectrum of the resonator as well as its quality factor. The assumption was to observe several undesired resonances suppressed as well as an increased quality factor. One of the main points one has to take into account when placing wire-bonds on a chip is the possibility to form superconducting loops that give rise to a magnetic field. If the loop is formed aroud a transmon qubit, a current flowing in this loop can tune the qubit transition frequency.

Chapter 2

Measurement Setup

To be able to measure the devices with different bond configurations a dipstick setup was used in the experiment. On the top of the dipstick are eight SMA connectors which are connected to an Agilent Technologies N5230C PNA-L 4 port network analyzer. The bottom has eight SMP connectors in a sample holder for direct connection and easy exchange of the sample. New cables from SMA to SMP were made to overcome any further reflexions due to additional converters. The chip is dipped in liquid helium, which takes about 15 minutes to fully cool down the sample. This setup has several advantages:

- Fast cooling of the sample to 4 K
- Fast exchange of the sample possible
- Superconducting niobium at 4 K

On the other hand there are downturns, namely the aluminium wire-bonds do not reach the superconducting state due to its critical temperature $T_C = 1.2K$ which is below the liquid helium temperature. The possibility of a different behaviour down at a few mK can also not be totally excluded. For example at a few mK the quality factors could be as high as Q $\sim 10^6$ if dominated by the internal Q.

The calibration of the measurement setup was done using an automatic calibration kit. It was calibrated between the different cables of the network analyzer. This means that we calibrated the cables from the network analyzer to the dipstick, but not the cables and connectors of the dipstick itself. This obviously will give rise to reflexions and losses which have to be taken into account.

Chapter 3

Resonator Beamsplitter

3.1 Stages of bonding

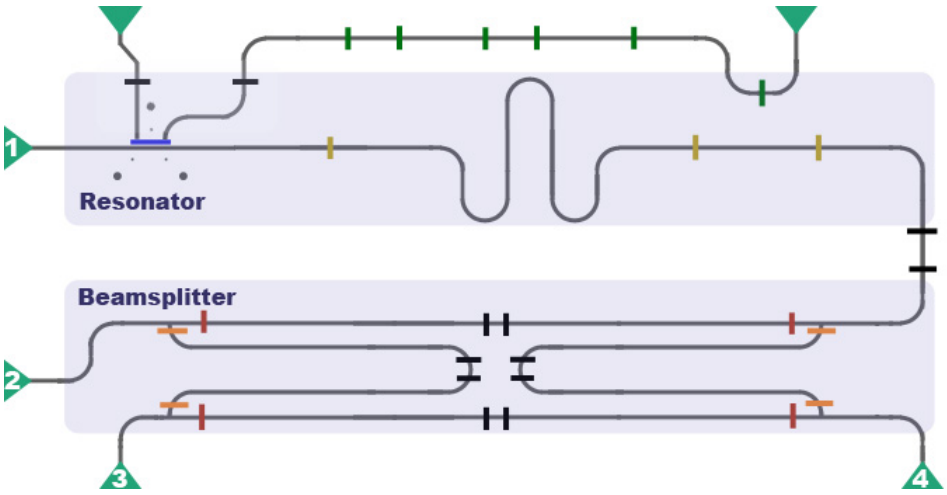

Figure 3.1: Schematic illustration of a resonator in series with a beamsplitter and a transmon qubit coupled to the resonator.

The first examined sample is a resonator in series with a beamsplitter. IT was looked at the S-parameters between the four ports labeled corresponding to the input port of the resonator (1) and output ports of the beamspitter (3,4), see Fig. 3.1. In five steps several bond-wires were attached to study their influence on the properties of the chip.

- First stage (black): eight bonds in the middle of the beamsplitter, one bond over each charge line to the transmon qubit and two bond between the resonator and the beamsplitter
- Second stage (green): six bonds over the long charge line of the transmon qubit
- Third stage (yellow): three bonds over the resonator

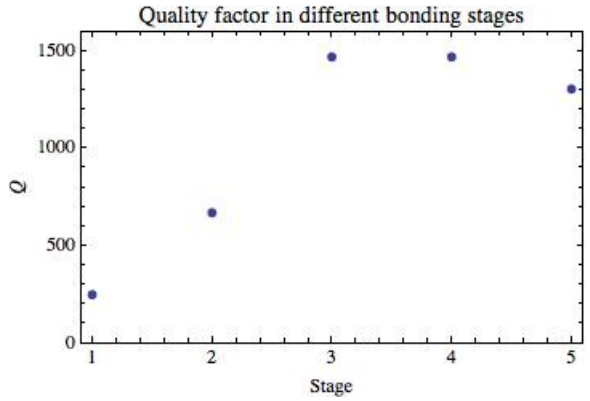

Figure 3.2: Different bonding stages according to the ones described in Sec. 3.1.

- Fourth stage (orange): four bond at the beamsplitter edges
- Fifth stage (red): four additional bonds at the beamsplitter edges

3.2 Measurement

In the measurements presented below if not mentioned differently the transmission between the input port (1) and the transmission port (4) is looked at.

3.2.1 Q factor measurements

To characterize the resonator in the resonator beamsplitter chip the fundamental frequency of the resonator was analysed while adding wire-bonds to the setup. The result can be seen in Fig. 3.2.

Additionally to the increasing Q factor with the additional wire-bonds at different places on the chip, the spectrum apparently cleared out. Especially near the fundamental frequency two resonances were observed in the beginning, but they cleared out in the third bonding stage, the bonds over the beamsplitter edges. This lets us conclude that the ground planes in the middle of the beamsplitter and especially its extremities are difficult to get to the same voltage level as the surrounding ground planes. This results in additional resonances. Furthermore a stagnation of the increase in the Q value with the third bonding stage is seen. In a closer look at the full spectra the importance of the third bonding stage is examined more closely.

3.2.2 Full spectrum view in different stages

Due to the results obtained form the Q factor analysis is split the full spectrum analysis into two parts. First the results from the the first three stages are analysed up to the saturation of the Q factor. Subsequently the third to the fifth stages are compared to each other. See Fig. 3.3 for the results of the measurements.

The first thing that jumps into ones eye is that the third bonding stage clears the spectrum around the fundamental resonance between 6 and 8 GHz.

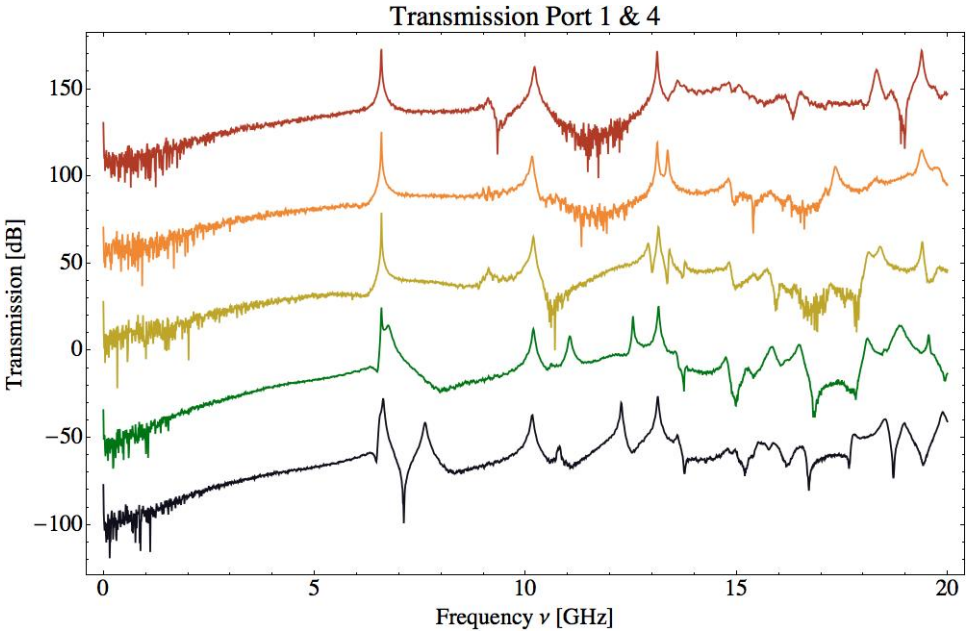

Figure 3.3: Full spectrum view of the resonator beamsplitter chip. The color scheme is according to the different stages in Sec. 3.1. (Black → first stage, green → second stage (+50 dB offset), yellow → third stage (+100 dB offset), orange → fourth stage (+150 dB offset), red → fifth stage (+200 dB offset))

The additional resonance shifted from the first to the second stage to a lower frequency and disappeared totally in the third and all following bonding stages. On the other hand a new resonance is observed at 9.15 GHz but with a much lower amplitude. It is possible that this is the same resonance as observed before but now shifted to a higher frequency. Over all a smoother spectrum up to 12 GHz compared to the first and second stage can be observed. In the area over 12 GHz the spectrum gets undefinable and it is difficult to draw any conclusions.

For the fourth and fifth bonding stages a very similar spectrum up to the 10.2 GHz resonance is seen but a lower transmission between the 10.2 GHz resonance and the 13.1 GHz resonance. Furthermore in the fourth bonding stage the additional peak at 12.9 GHz disappears and in the fifth stage also the one at 13.4 GHz shifts to lower amplitude and a higher frequency.

Over all the spectrum above 13 GHz is very difficult to characterize and smoothen. Up to 13 GHz a big improvement with the third bonding stage is seen. For a further improvement in the range of 10 to 13 GHz the fourth and fifth bonding stages can be crucial.

In App. A.1 the plots between the other ports of the resonator beamsplitter sample are shown. The transmission between the input port (1) and the two output ports (3,4) is not perfectly symmetric as expected. But the spectra between the input and the three other ports (vacuum, and the two output ports) are very similar and also evolve with the bonding in a similar way. With the additional bond a vanishing of several resonances is observed.

Chapter 4

Multi Q resonator

In this chapter a resonator with a transmon qubit on either end and additional two ports in the middle of the resonator is examined. This sample is also called a multi Q resonator.

4.1 Stages of bonding

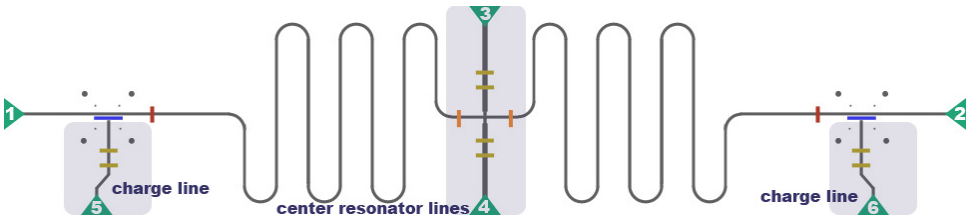

Figure 4.1: Schematic illustration of the multi Q resonator with two transmon qubits.

To analyse the influence of the wire-bonds on the circuit its properties were measured in different stages. In Fig. 4.1 the five different stages described below are graphically shown.

- First stage (black): no bonds and without a sample cover, all following stages are with the use of a sample cover
- Second stage (green): no bonds were on the chip
- Third stage (yellow): two wire-bonds over each center resonator line and two wire-bonds over each qubit charge line
- Fourth stage (orange): Two bonds in the middle of the resonator, symmetrically placed
- Fifth stage (red): Two bonds over the resonator next to the transmon qubit

Those wire-bonds seemed the most reasonable at the time of the experiment to achieve the highest possible symmetry in the ground planes. The ground planes are represented in white in Fig. 4.1 and it is split into six parts which are individually grounded to an outside ground level with several wire-bonds each. Compared to the two ground planes in a simple resonator setup this gives rise to undesired resonances and is the main problem adressed in this report. Grey is the coplanar waveguide and in green are the six different ports. Colored in blue are the transmon qubit placeholders.

4.2 Measurements

The presented measurements are the resonator transmission between port 1 and 2 if not stated differently.

4.2.1 Quality factor measurement

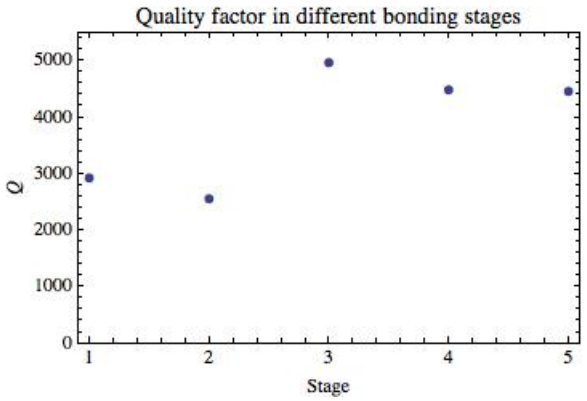

Figure 4.2: Quality factor measurements for the five different stages as described in section 4.1.

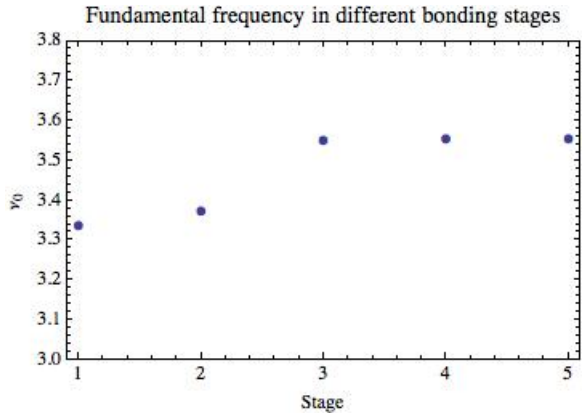

Figure 4.3: Fundamental frequency ν_0 in the different stages.

One of the main characteristics of a coplanar waveguide resonator is the quality factor (Q). The quality factor affiliate to the fundamental resonance of the full resonator (port 1 and 2 in Fig. 4.1) was measured at each stage. Additional to the different bonding states the quality factor for the sample was also analysed with and without a sample cover (first and second stage) before the sample was bonded. All following measurements with bonds were done using the sample cover.

There are three observations which can be made from this simple quality factor analysis which can be seen in Fig. 4.2.

- The third stage where the first bonds were introduced which were placed over the flux lines as well as the charge lines in the middle of the resonator resulted in almost a doubling of the quality factor of the resonator.
- The sample cover slightly decreases the quality factor, but on the other hand gets rid of the sample holder resonances around 6 GHz, see Fig. 4.5.
- As expected we observe a saturation of the quality factor after the attachment of the first bonds.

The fundamental frequency ν_0 does shift with the sample cover as well as with attaching wire-bonds to the chip, see Fig. 4.3. Interestingly the shift only happens once and the fundamental frequency does not shift any further with the attaching of more wire-bonds.

4.2.2 Power dependance

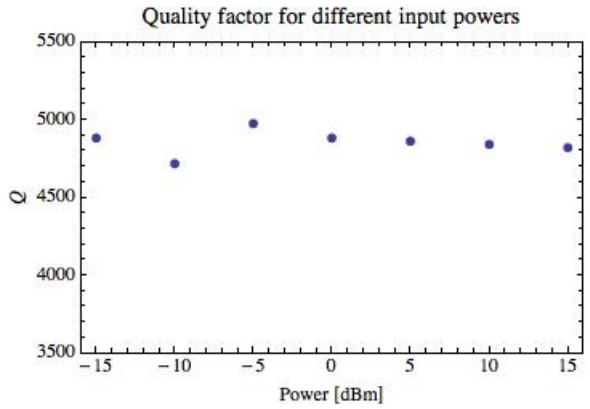

Figure 4.4: Quality factor obtained from a Lorentz fitting of the fundamental resonance frequency of the resonator at input powers from -15 dBm to +15 dBm.

For a more detailed result the input power was varied from the initial -15 dBmin 5 dBm steps up to 15 dBm. Those measurements were done in the third stage where bonds over the charge lines and the center resonator lines (yellow) were attached to the chip. It lead to better results in terms of zero level transmission. The fundamental frequency of the resonator did not shift with the power variation. But a small variation in the quality factor can be observed. The

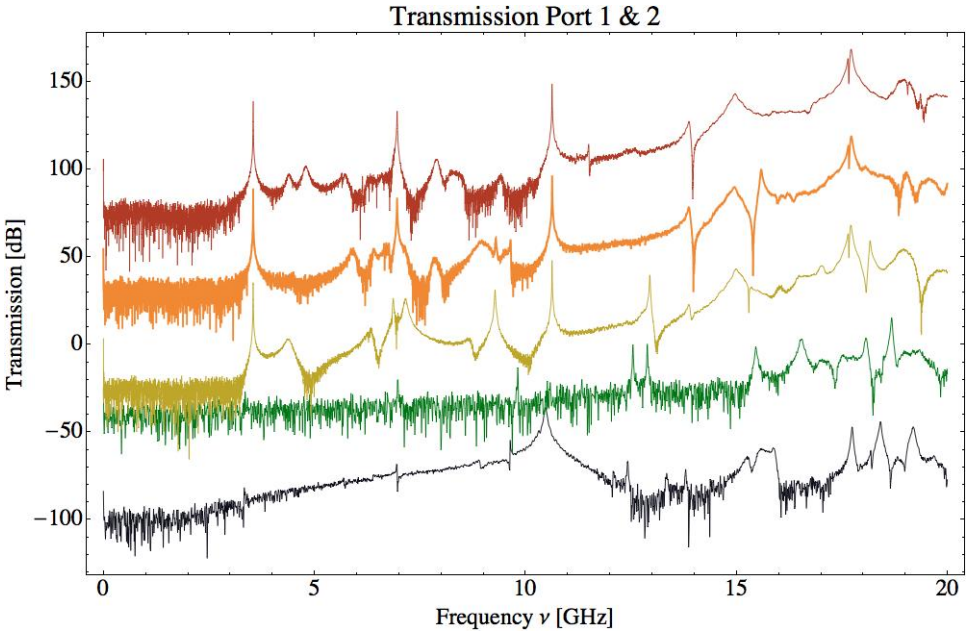

Figure 4.5: Full spectrum view of transmission line resonator between port 1 and 2. The color scheme is according to the stages Sec. 4.1.(Black → first stage, green → second stage (+50 dB offset), yellow → third stage (+100 dB offset), orange → fourth stage (+150 dB offset), red → fifth stage (+200 dB offset))

mean value of the quality factor is $Q = 4851 \pm 76$. This result was obtained with the same fitting parameters for every measurement and the result could be optimised with individual adjusting of the fitting parameters. This could be the explanation for the two outliner quality factors for -10 dBm and -5 dBm. Fig. 4.4 shows the individual Q values obtained for the different input power settings.

From the full view analysis a new frequency arising at 4.45 GHz is observed with additional power input. Due to the lower noise level at higher power a lowering in the zero level transmission up to 10 dBm could be observed. The influence of any further bond-wires were analysed using 10 dBm input power.

4.2.3 Full spectrum view with different bondings

The main reason of the investigation was to closely observe the full spectrum up to 20 GHz of the multi Q resonator. Due to the wire-bonds it is possible that new resonances would be observed or that certain resonances are suppressed.

In the full spectrum view, Fig. 4.5, it can be seen that the sample holder resonances around 5.5 to 6.5 GHz disappear through the use of a sample cover. Furthermore does the third bonding stage (the first to use any bonds) smoothen out the spectrum up to almost 14 GHz. Above 14 GHz the spectrum is difficult to define.

In the forth and especially the fifth stage the frequency clearly visible in the third stage at 4.8 GHz shifts up to higher frequency and almost disappears in

the fifth bonding stage. Furthermore the undesired peak around 9.5 GHz which appears in the third as well as the fourth stage disappears in the fifth one. On the other side an additional resonance shows up around 11.5 GHz which must be due to the new bonds attached.

In App. A.2 the plots between the other ports of the resonator beamsplitter sample are shown. The main results are summarized here.

- Generally the spectra between the fundamental and the first harmonic resonance of the resonator smoothens up to the third stage but gets worse with the additional bonds in the fourth and fifth stage.
- The sample holder resonance can be observed around 5.5 to 6.5 GHz disappear in almost all the spectra.
- Resonances occurring around 9 to 10 GHz shift to 10.5 to 11.5 GHz in the fifth stage.

4.3 T_1 analysis

In a cryostat experiment with a multi Q resonator the decoherence time of the qubit (T_1) was measured. At 4.8 GHz an unexpected drop of T_1 occurred. Looking at the full spectrum of the multi Q resonator this could occur due to a coupling of the qubit to the resonance observed at that frequency. With a bonding set similar to the fifth bonding stage it could be observed if T_1 would increase at 4.8 GHz.

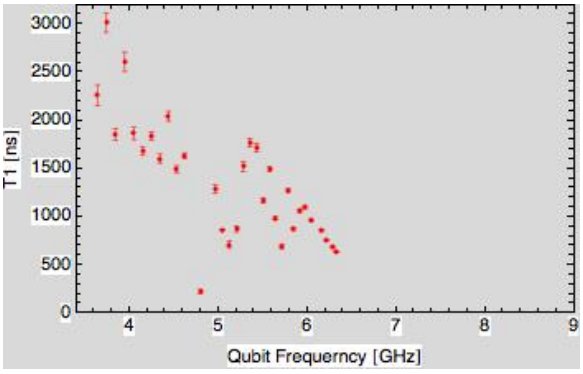

Figure 4.6: T1 measurements of a transmon qubit on a multi Q resonator in a cryostat.

Chapter 5

Conclusion and Outlook

5.1 Conclusion

Looking at two different samples the influence of wire-bonds was studied. Several questions were answered and a good data base built up which can be used to compare with results from cryostat experiments. From that it can be decided if an additional bonding might help to suppress certain resonances. The use and applicability to experiments at a few mK has yet to be proved but as shown in Sec. 4.3 there are possibilities of correlations.

The use of wire-bonds was shown in the experiment but it can not be drawn a general conclusion which bonds are important. This decision has to be made from case to case. The data accumulated in the experiment can be used for further decision taking in experiments.

5.2 Outlook

There are unanswered and new questions arising from the experiments done in this work. One interesting questions is the influence of the place where wire-bonds are placed on a chip. It is known that it is possible to form superconducting loops which give rise to magnetic fields. This has to be taken into account every time wire-bonds are attached to a chip.

There is also the possibility to design an air-bridge mask to add air-bridges to the same places for a scalable amount of chips. In accordance with experiments performed in a cryostat it should be possible to work out the essential bonds.

5.3 Acknowledgements

I would like to thank the whole team of the Quantum Device Lab for all the constructive discussions and for their friendly welcom into the group. Especially I would like to thank Prof. Andreas Wallraff for the possibility to work in his dynamic group. Furthermore my special thanks go to Lars Steffen who accompanied me through the whole process from the simple idea to the endresult.

Bibliography

[1] J. R. Powell, "The quantum limit to moore's law," *Proceedings of the IEEE*, vol. 96, pp. 1247–1248, August 2008.

[2] A. Hagar, "Quantum computing," February 2007. `http://plato.stanford.edu/entries/qt-quantcomp/`.

[3] G. S. E. et al., "Evidence for wavelike energy transfer through quantum coherence in photosynthetic systems," *Nature*, vol. 446, pp. 782–786, April 2007.

[4] B. Online, "Quantum computing," November 2007. `http://news.bbc.co.uk/2/low/technology/7085019.stm`.

[5] A. B. et al., "Cavity quantum electrodynamics for superconducting electrical circuits: An architecture for quantum computation," *Phys. Rev. A*, vol. 69, p. 062320, June 2004.

[6] A. W. et al., "Strong coupling of a single photon to a superconducting qubit using circuit quantum electrodynamics," *Nature*, vol. 431, pp. 162–167, September 2004.

[7] Y. N. et al., "Coherent control of macroscopic quantum states in a single-cooper-pair box," *Nature*, vol. 398, pp. 786–788, April 1999.

[8] M. H. D. et al., "Superconducting qubits: A short review," 2004.

[9] J. K. et al., "Charge-insensitive qubit design derived from the cooper pair box," *Phys. Rev. A*, vol. 76, p. 042319, Oct 2007.

[10] A. W. et al., "Superconducting solid state cavity quantum electrodynamcis." Internal notes on resonators, Yale, jan 2003.

[11] D. P. DiVincenzo, "Quantum computation," *Science*, vol. 270, no. 5234, pp. 255–261, 1995.

List of Figures

List of Tables

Appendix A

Additional Plots

A.1 Resonator Beamsplitter

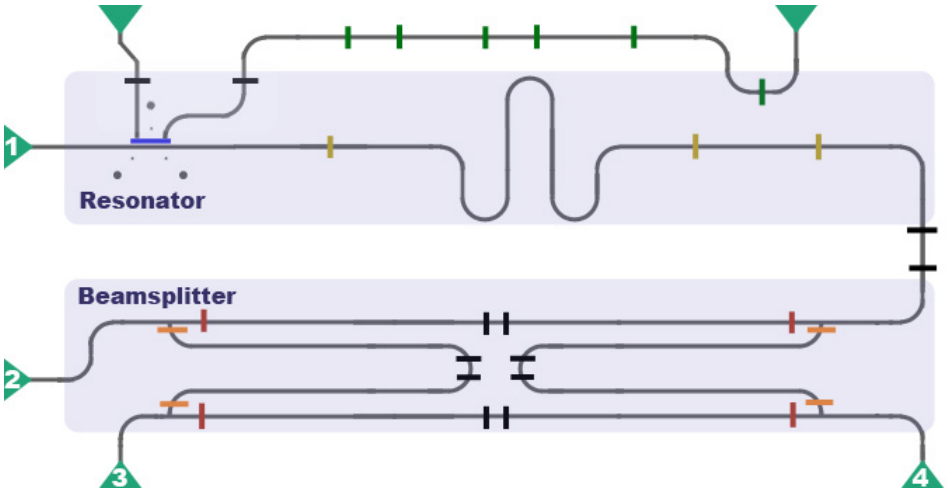

Figure A.1: Schematic illustration of a resonator in series with a beamsplitter and a transmon qubit coupled to the resonator.

All the plots below are with an offset of 50 dB between each dataset. The black dataset corresponding to the first stage is without offset.

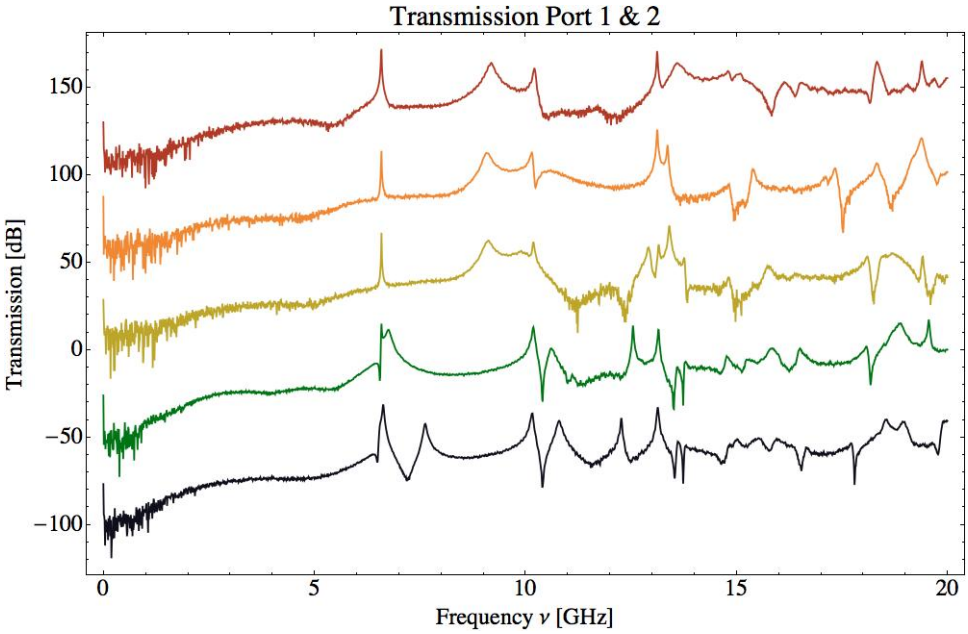

Figure A.2: Black → first stage, green → second stage (+50 dB offset), yellow → third stage (+100 dB offset), orange → fourth stage (+150 dB offset), red → fifth stage (+200 dB offset), see Fig A.1 and Sec. 3.1.

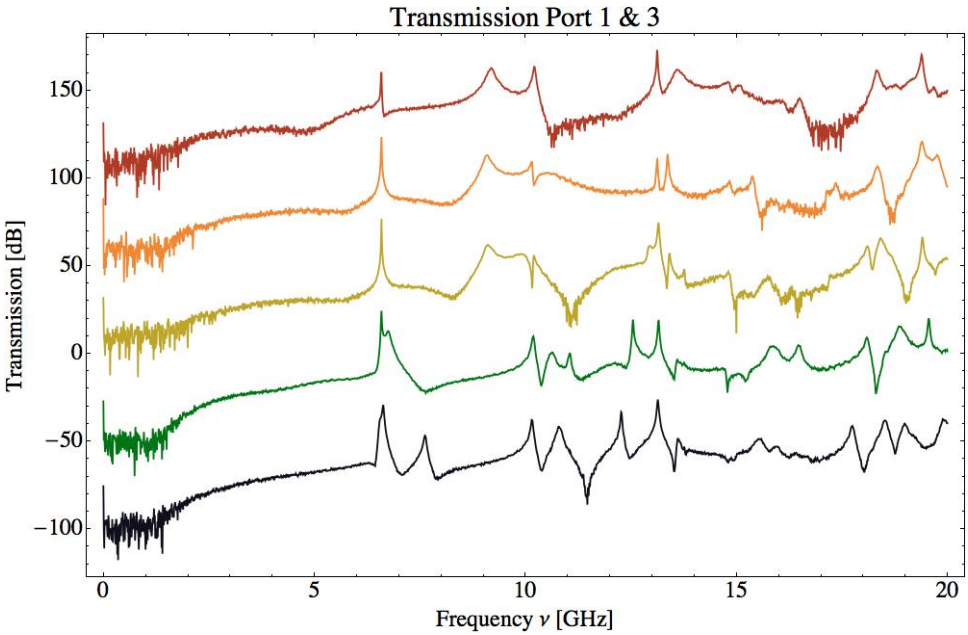

Figure A.3: Black → first stage, green → second stage (+50 dB offset), yellow → third stage (+100 dB offset), orange → fourth stage (+150 dB offset), red → fifth stage (+200 dB offset), see Fig A.1 and Sec. 3.1.

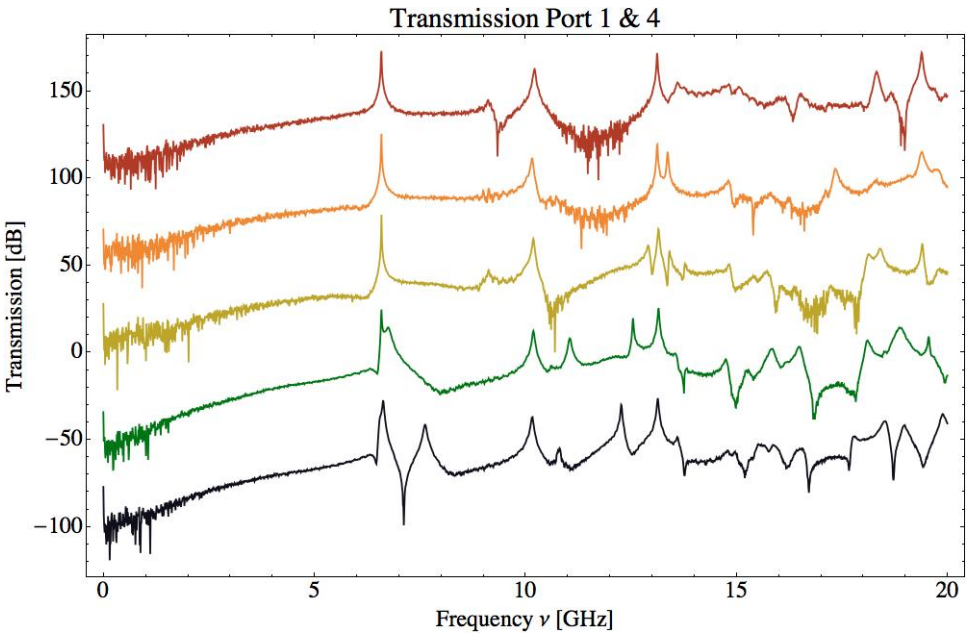

Figure A.4: Black → first stage, green → second stage (+50 dB offset), yellow → third stage (+100 dB offset), orange → fourth stage (+150 dB offset), red → fifth stage (+200 dB offset), see Fig A.1 and Sec. 3.1.

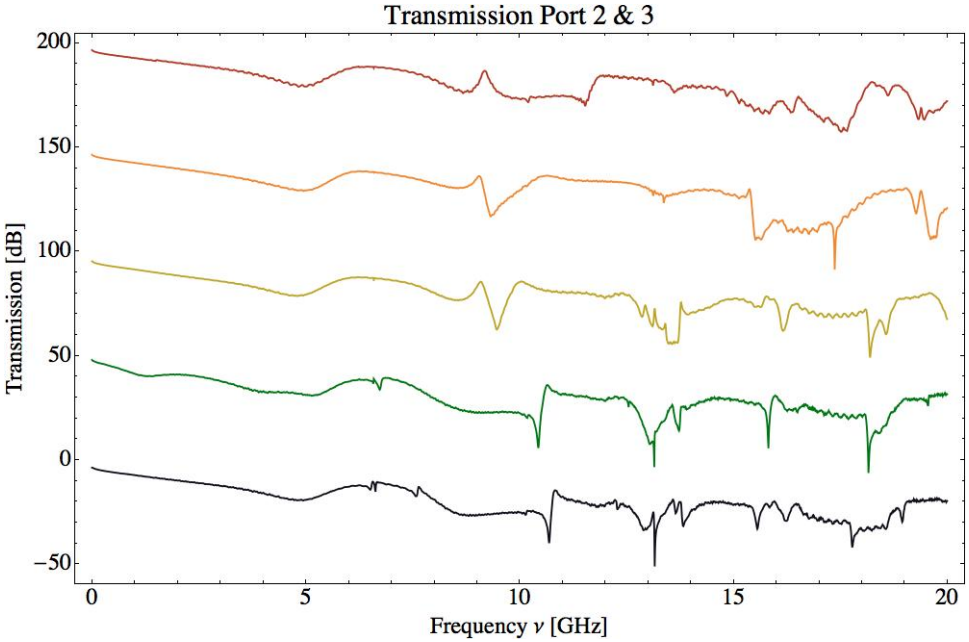

Figure A.5: Black → first stage, green → second stage (+50 dB offset), yellow → third stage (+100 dB offset), orange → fourth stage (+150 dB offset), red → fifth stage (+200 dB offset), see Fig A.1 and Sec. 3.1.

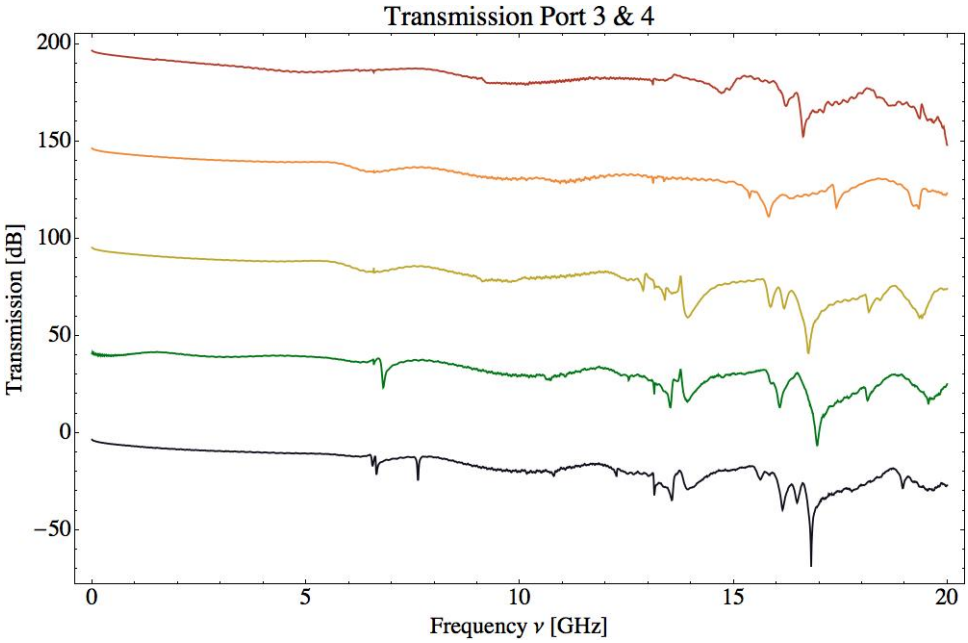

Figure A.6: Black → first stage, green → second stage (+50 dB offset), yellow → third stage (+100 dB offset), orange → fourth stage (+150 dB offset), red → fifth stage (+200 dB offset), see Fig A.1 and Sec. 3.1

A.2 Multi Q resonator

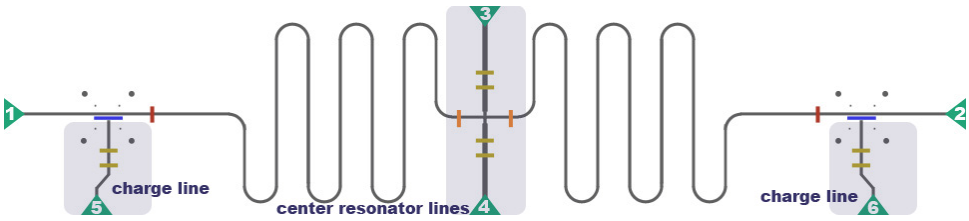

Figure A.7: Schematic illustration of the multi Q resonator with two transmon qubits.

All the plots below are with an offset of 50 dB between each dataset. The black dataset corresponding to the first stage is without offset.

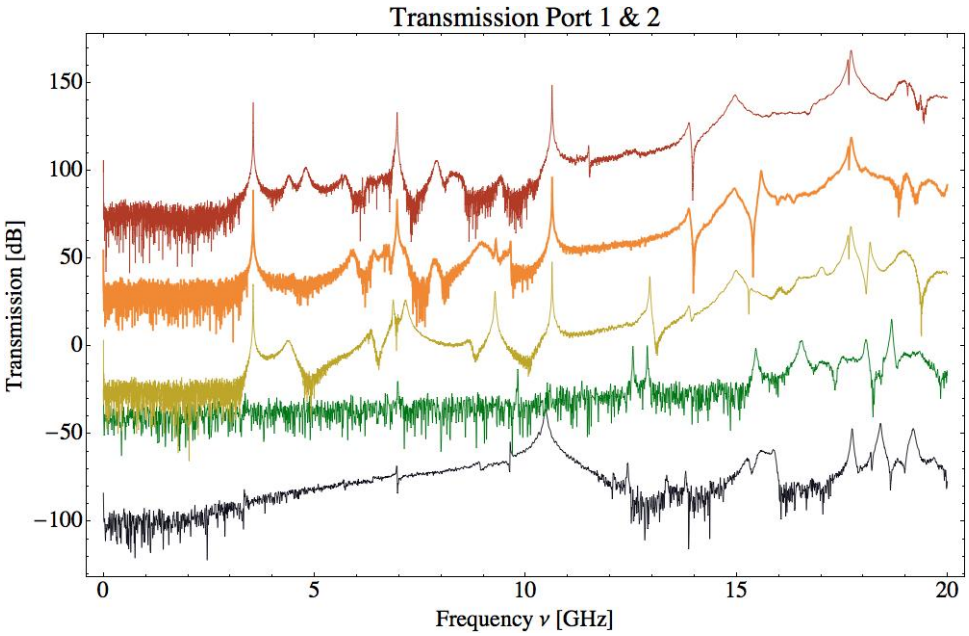

Figure A.8: Black → first stage, green → second stage (+50 dB offset), yellow → third stage (+100 dB offset), orange → fourth stage (+150 dB offset), red → fifth stage (+200 dB offset), see Fig A.7 and Sec. 4.1.

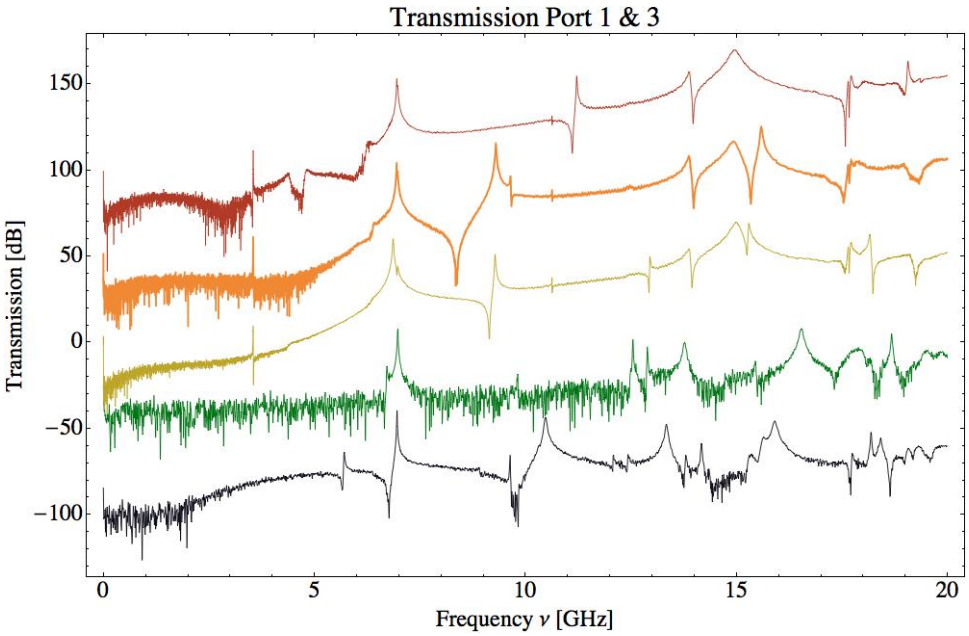

Figure A.9: Black → first stage, green → second stage (+50 dB offset), yellow → third stage (+100 dB offset), orange → fourth stage (+150 dB offset), red → fifth stage (+200 dB offset), see Fig A.7 and Sec. 4.1.

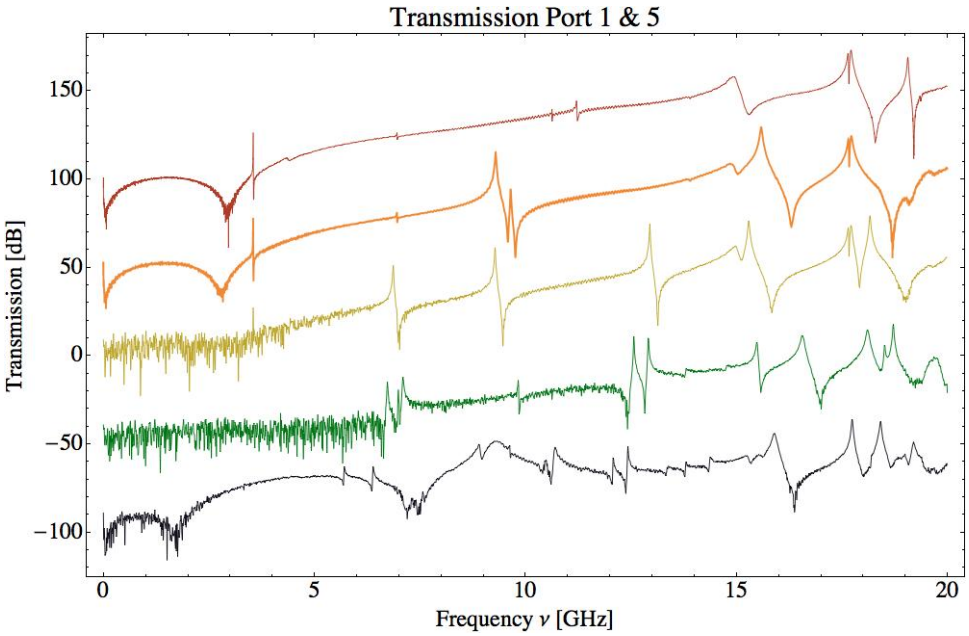

Figure A.10: Black → first stage, green → second stage, yellow → third stage, orange → fourth stage, red → fifth stage, see Fig A.7 and Sec. 4.1.

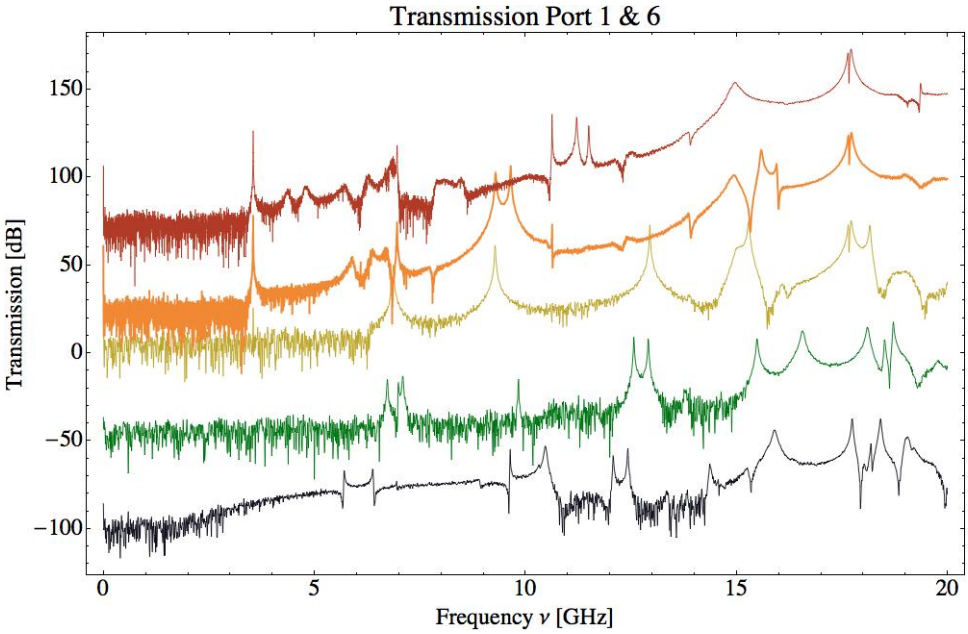

Figure A.11: Black → first stage, green → second stage (+50 dB offset), yellow → third stage (+100 dB offset), orange → fourth stage (+150 dB offset), red → fifth stage (+200 dB offset), see Fig A.7 and Sec. 4.1.

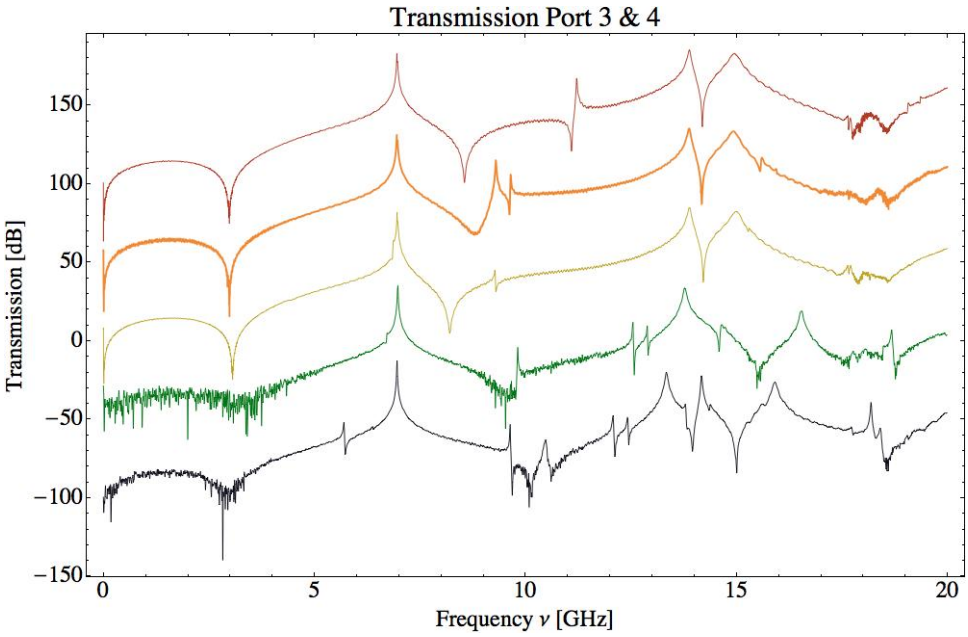

Figure A.12: Black → first stage, green → second stage (+50 dB offset), yellow → third stage (+100 dB offset), orange → fourth stage (+150 dB offset), red → fifth stage (+200 dB offset), see Fig A.7 and Sec. 4.1.

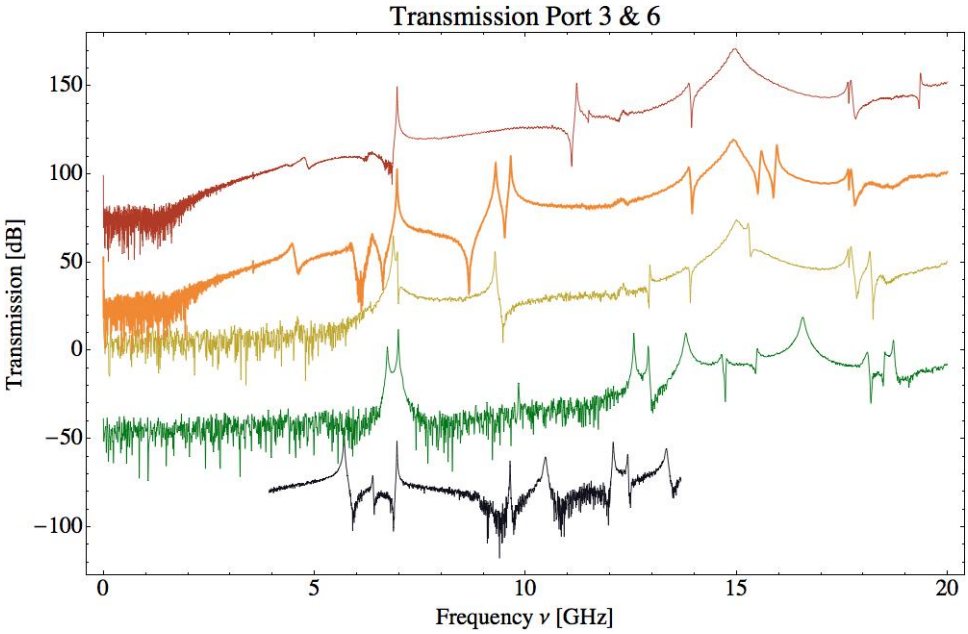

Figure A.13: Black → first stage, green → second stage (+50 dB offset), yellow → third stage (+100 dB offset), orange → fourth stage (+150 dB offset), red → fifth stage (+200 dB offset), see Fig A.7 and Sec. 4.1.

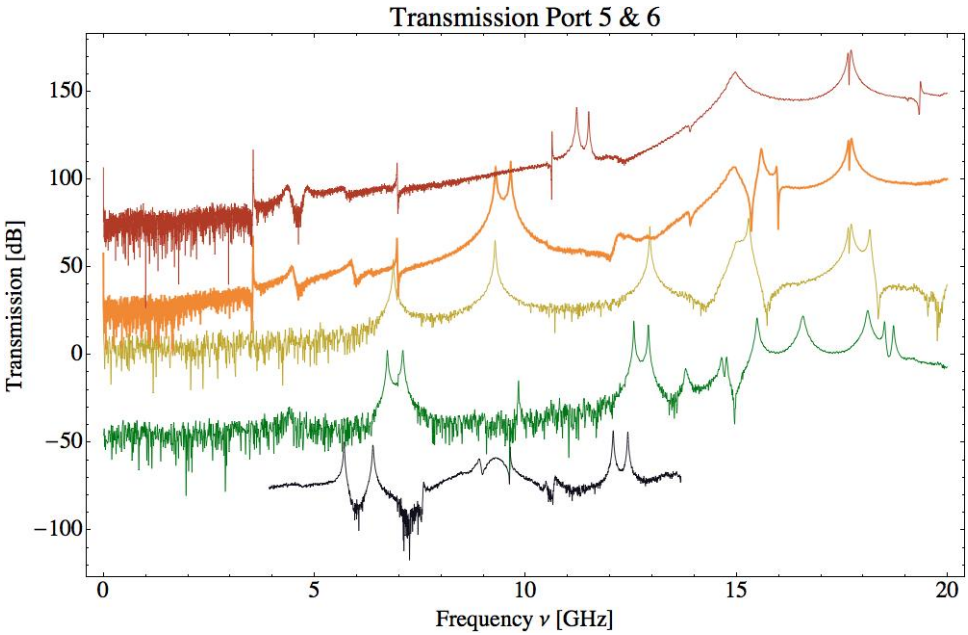

Figure A.14: Black → first stage, green → second stage (+50 dB offset), yellow → third stage (+100 dB offset), orange → fourth stage (+150 dB offset), red → fifth stage (+200 dB offset), see Fig A.7 and Sec. 4.1.